



Synergy between Fe and Mo single atom catalysts for ammonia electrosynthesis

Jieying Wan^a, Hao Zhang^{a,*}, Ji Yang^{b,*}, Jiageng Zheng^a, Zhongkang Han^c, Wentao Yuan^c, Bingru Lan^a, Xiaodong Li^{a,*}

^a State Key Laboratory of Clean Energy Utilization, Zhejiang University, Hangzhou 310027, China

^b Collaborative Innovation Center of Chemistry for Energy Materials (iChEM), College of Chemistry and Chemical Engineering, Xiamen University, Xiamen 361005, China

^c School of Materials Science and Engineering, Zhejiang University, Hangzhou 310027, China

ARTICLE INFO

Keywords:

Ammonia synthesis
Electrochemical nitrate reduction reaction
Tandem mechanism
Dual single atom catalyst
In-situ characterization

ABSTRACT

Electrochemical nitrate to ammonia conversion provides an eco-friendly route for a highly valued product. However, nitrite intermediate formation and hydrogen evolution competition hinder full conversion. Here, we implement a Fe-Mo dual single-atom catalyst where the two metals work in tandem to achieve nitrate to ammonia conversion with excellent activity and stability, an ammonia yield rate of up to 13.56 mg cm⁻² h⁻¹ and a Faradaic efficiency up to 94%. In-situ Raman and Fourier-transform infrared spectroscopy confirms nitrite as the intermediate bound to metal sites. Time-dependent detection of products and DFT calculations support a tandem mechanism: the Mo single atoms are the preferred sites for the conversion of nitrate to nitrite, while the Fe single atoms catalyze the further conversion of nitrite to ammonia. This discovery paves the way for energy-relevant transformations using bimetallic single-atom catalysts.

1. Introduction

NH₃ is one of the most extensively produced chemicals as it is a vital raw material for fertilizers [1–5]. It is also increasingly recognized as an attractive carbon-neutral hydrogen and energy carrier [6–8]. However, the industrial Haber-Bosch process for NH₃ production consumes up to 1–3% of the global energy supply and produces about 400 Mt CO₂ emissions every year [9–14]. As an alternative, environmentally friendly electrocatalytic N₂ reduction reaction (NRR) [14,15] in water has attracted broad attention due to the use of water, instead of natural gas, as the hydrogen source and the potential to use electricity sourced from solar radiation or wind [15]. Nevertheless, the negligible water solubility of N₂ and the high dissociation energy of the N≡N bond (941 kJ mol⁻¹) strongly limit the energy efficiency of NRR [14,16,17]. By contrast, among N-containing species, NO₃⁻ exhibits a relatively low dissociation energy of the N = O bond (204 kJ mol⁻¹) and excellent water solubility, which enable NO₃⁻ as a promising nitrogen source for aqueous electrochemical NH₃ production under ambient conditions [18–20]. Moreover, benefiting from recent advances in gas conversion technologies such as non-thermal plasma conversion, NO₃⁻ can be

efficiently obtained directly from air with low cost [21–23]. Electrochemical NO₃⁻ reduction reaction (NO₃RR) can be used to further upconvert NO₃⁻ to value-added NH₃.

Nevertheless, NO₃RR involves a complex coupled transfer of eight electrons and nine protons (NO₃⁻ + 6 H₂O + 8e⁻ → NH₃ + 9OH⁻ in alkaline solution), which leads to sluggish kinetics for NH₃ synthesis [24,25]. Previous reports demonstrated that, for some monometallic catalysts (e.g., Cu, Rh, Pd, and Pt) for NO₃⁻ reduction, the hydrogenation of NO₂⁻ to NH₃ is the rate-limiting process at lower overpotentials due to its lower rate than that of NO₃⁻-to-NO₂⁻ conversion. As a result, *NO₂ desorbs from catalyst surface and NO₂⁻ accumulates in the electrolyte [26–28]. For instance, Cu-based catalysts tend to produce NO₂⁻ instead of NH₃, with a FE of nearly 100% at 0 V vs. the reversible hydrogen electrode (RHE) [29]. Further hydrogenation of produced NO₂⁻ is quite limited at low overpotentials because of the low availability of active hydrogen (*H) [30]. Higher overpotentials can allow the dissociation of water to form *H promoting successive deoxygenation and hydrogenation of NO₂⁻ at a higher rate than that of NO₃⁻-to-NO₂⁻ conversion [28,31]. However, under such potentials, HER dominates effectively out-competing with NO₃⁻ reduction and leading to sluggish or incomplete

* Corresponding authors.

E-mail addresses: zhang_hao@zju.edu.cn (H. Zhang), chem.yang@xmu.edu.cn (J. Yang), lixid@zju.edu.cn (X. Li).

<https://doi.org/10.1016/j.apcatb.2024.123816>

Received 19 September 2023; Received in revised form 2 February 2024; Accepted 3 February 2024

Available online 6 February 2024

0926-3373/© 2024 Elsevier B.V. All rights reserved.

reduction of NO_3^- and thereby low selectivity for NH_3 [27]. Ultimately, the challenge with monometallic catalysts is that they do not simultaneously catalyze NO_3^- -to- NO_2^- and NO_2^- to- NH_3 conversion because the optimization of one of these reactions leads to sub-optimal activity for the other.

To overcome these challenges, in this work, a Fe-Mo dual single atom catalyst (Fe-Mo DSAC) was designed and implemented to realize NO_3RR through a tandem two-stage pathway. To the best of our knowledge, there are only a few reports of NO_3RR to NH_3 over DSACs. We studied the electrocatalytic NO_3RR activity of the Fe-Mo DSAC by in-situ Raman spectroscopy, in-situ Fourier transform infrared (FTIR) spectroscopy, time-dependent detection of nitrogen-containing products, and density functional theory (DFT) calculations. The finding of NO_2^- , an intermediate in the conversion of NO_3^- to NH_3 , reveals a tandem mechanism: the reduction of NO_3^- to NO_2^- is preferentially catalyzed on Mo single atoms, however further hydrogenation is suppressed; the Fe single atoms continue the cascade by catalyzing the conversion of the NO_2^- intermediate to NH_3 . Consequently, Fe-Mo DSAC exhibited a NH_3 yield rate of up to $13.56 \text{ mg cm}^{-2} \text{ h}^{-1}$ and a FE up to 94% in 0.1 M NO_3^- . These performance metrics surpass those of many reported catalysts for NO_3RR .

2. Results and discussions

2.1. Synthesis and characterization of Fe-Mo DSAC

The Fe-Mo DSAC was prepared by a facile pyrolysis-mechanical agitation synthesis strategy [32], as shown in Fig. 1a. The first step involves pyrolysis of the precursors at 650°C to obtain a Mo SAC [33], then iron phthalocyanine (FePc) was atomically loaded on the Mo SAC by mechanical agitation at room temperature ("Methods"). The as-synthesized Fe-Mo catalyst features an open porous structure (Fig. S1 in the Supplemental Information (SI)) and high surface area ($366.6 \text{ m}^2/\text{g}$, Fig. S2), both of which ascertain high accessibility of active sites

and facile mass transport during electrochemical NO_3^- reduction.

Additionally, elemental maps of the Fe-Mo DSAC by energy-dispersive X-ray spectroscopy (EDS) confirm the homogeneous distributions of Fe, Mo, N, and C throughout the entire N-doped carbon structure (Fig. 1b–f). Similarly, Fe and Mo SAC also presented a good dispersion of atomic species (Fig. S3–S4). The absence of metallic crystallites in these as-synthesized catalysts is in line with the mere presence of low-crystallinity graphitic property in X-ray diffraction (XRD) patterns (Fig. S5) and is indicative of the high atomic dispersion of Fe and Mo species on the N-C substrate. Moreover, the atomic Fe and Mo concentration in the Fe-Mo DSAC is 0.8 wt% and 5.2 wt%, respectively, as confirmed by inductively coupled plasma optical emission spectroscopy (ICP-OES, Table S1). The single-atom dispersion of Fe and Mo species is verified by aberration-corrected high-angle annular dark-field scanning transmission electron microscopy (HAADF-STEM) in Fig. 1g and Figs. S6–S8.

X-ray absorption near-edge structure (XANES) and extended X-ray absorption fine structure (EXAFS) spectra were employed to investigate the chemical states and coordination environment of Fe and Mo atoms (Fig. 2). Fe and Mo K-edge XANES profiles of the Fe-Mo DSAC (Fig. 2a–b) illustrate that the valence states of Fe and Mo are +2 to +3 and +4 to +6, respectively. This information is consistent with the findings of XPS analysis (Fig. S9–S11). Moreover, the XANES profiles of Fe and Mo K-edge in Fe-Mo DSAC are similar to those of the Fe and Mo SAC, respectively, indicating that the electronic states and spatial configuration of Fe and Mo centers inherit from Fe/Mo SAC. In fact, the analogous microenvironment of Fe or Mo centers within SAC and DSAC could be well comprehended due to the pyrolysis-free synthetic approach after loading FePc at room temperature.

The coordination environment of the Fe and Mo atoms in as-prepared catalysts was investigated by EXAFS. The Fourier-transformed (FT) Fe K-edge EXAFS profiles of the Fe-Mo DSAC and the Fe SAC (Fig. 2c) show a dominant peak around 1.6 \AA , which can be assigned to Fe-N coordination. There is a negligible contribution from the Fe-Fe bond peak

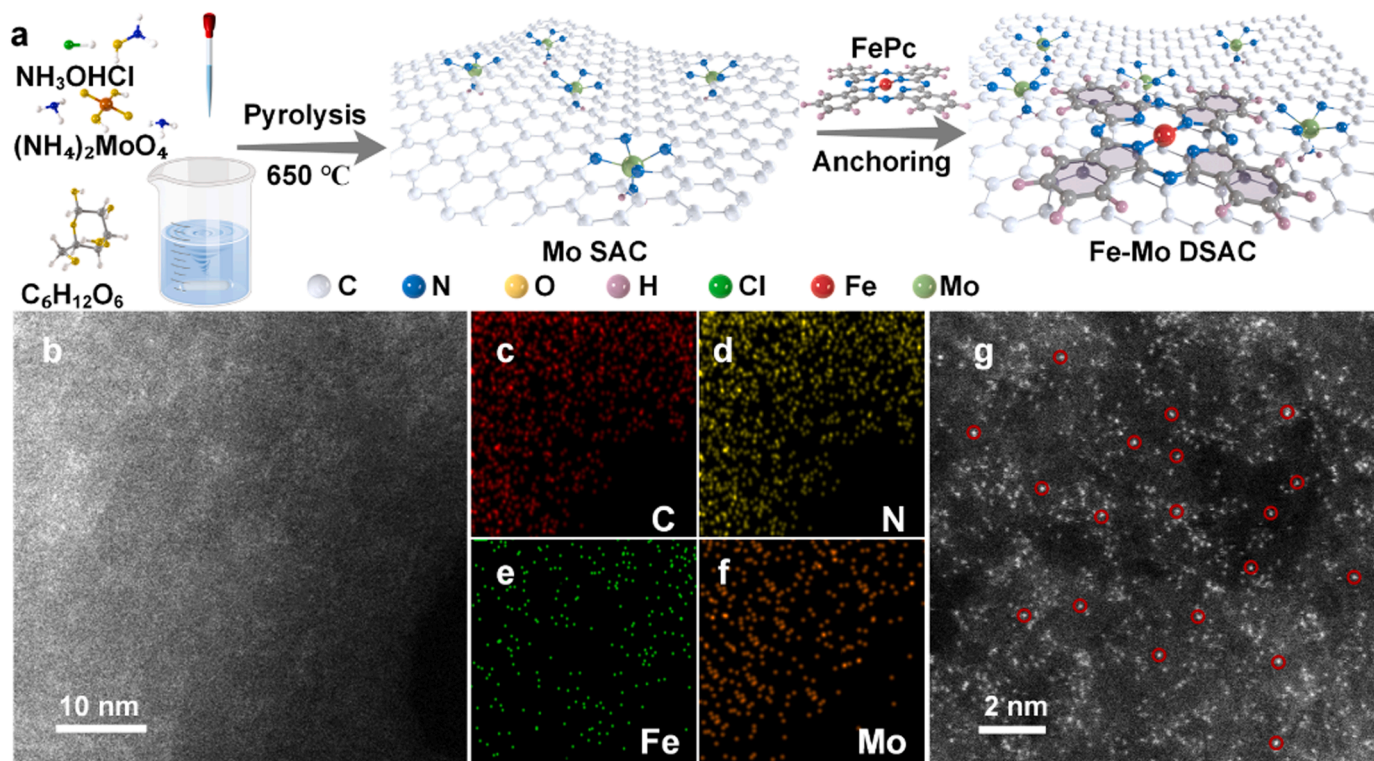


Fig. 1. Synthesis and characterization of Fe-Mo DSAC: (a) Schematic illustration of the two-step synthesis process. (b) Scanning transmission electron microscopy (STEM) image and corresponding element maps of (c) C, (d) N, (e) Fe and (f) Mo. (g) Atomic-resolution HAADF-STEM image.

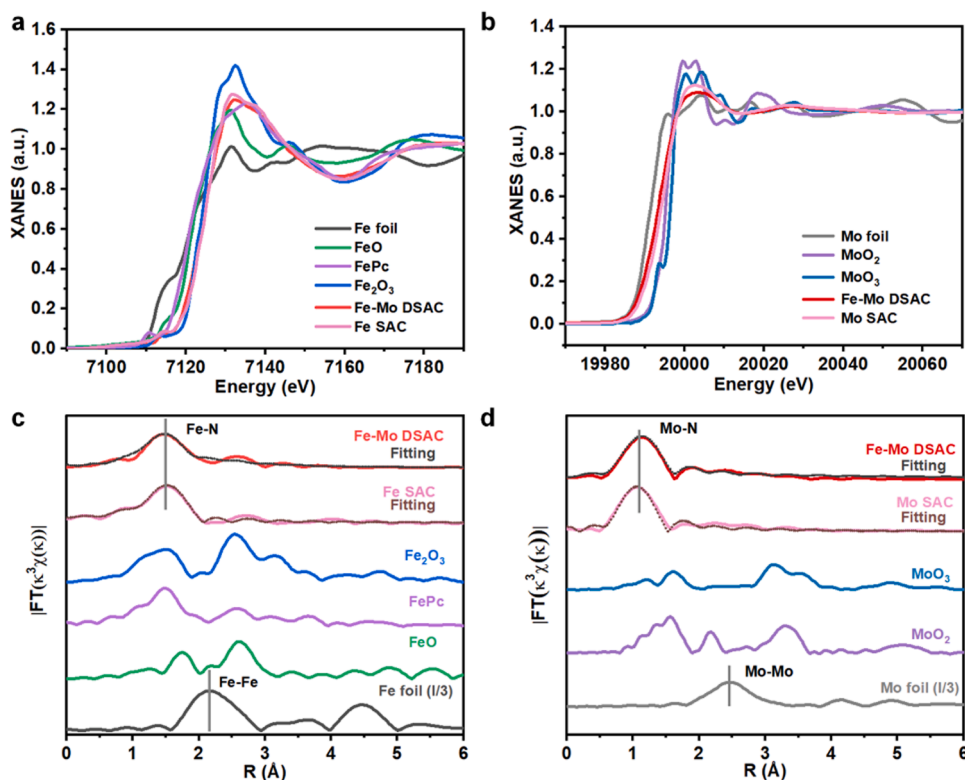


Fig. 2. (a) XANES spectra at the Fe K-edge of the Fe-Mo DSAC and Fe SAC. (b) XANES spectra at the Mo K-edge of the Fe-Mo DSAC and Mo SAC. (c) FT K^3 -weighted $\chi(k)$ -function of the EXAFS spectra at Fe K-edge of the Fe-Mo DSAC, Fe SAC and fitting results of the EXAFS spectra of the Fe-Mo DSAC, Fe SAC at Fe K-space. (d) FT K^3 -weighted $\chi(k)$ -function of the EXAFS spectra at Mo K-edge of the Fe-Mo DSAC, Mo SAC and fitting results of the EXAFS spectra of the Fe-Mo DSAC, Mo SAC at Mo K-space.

expected at 2.2 Å [34–36], further excluding the existence of any Fe clusters or nanoparticles in the catalysts. Similarly, for Mo atoms (Fig. 2d), the strongest peak is centered at approximately 1.2 Å, which is attributable to Mo-N contribution, while the Mo-Mo bond peak expected at 2.6 Å is not observed [33,37], suggesting that the Mo atoms in the Fe-Mo DSAC and the Mo SAC are bonded with N. These results show that the Fe and Mo atoms are atomically dispersed over the N-doped carbon substrate, consistent with STEM observations. The EXAFS fitting results (Fig. 2c–d) show similar coordination numbers for Fe or Mo atoms in different catalysts. Each Mo atom is coordinated by about five N atoms on average while Fe atom is coordinated by four N atoms, illustrating that FePc is linked with the N-doped carbon substrate through a π bond [38,39]. These characterizations show that the Fe-Mo DSAC, Fe SAC, and Mo SAC possess Fe-N₄ and Mo-N₅ coordination. The similar electronic state and atomic configuration indicates that the local atomic structure around Fe and Mo metal atoms in the DSAC is identical to that in their SAC analogues. In order to further illustrate the valence states of Fe and Mo in the catalysts by the XANES spectra at the Fe K-edge, a comparison of E_0 values (the first inflection point) shows that Fe-Mo DSAC has an E_0 value of 7123.7 eV, as well as Fe SAC (7123.6 eV), which is between that of the FeO and Fe₃O₄ references (Table S5). It suggests the coexistence of Fe²⁺ and Fe³⁺ in Fe-Mo DSAC and Fe SAC, which is consistent with XPS analysis. Similarly, in the XANES spectra at the Mo K-edge, Fe-Mo DSAC and Mo SAC have E_0 values of 20015.7 eV and 20015.5 eV (Table S5), which is between MoO₂ and MoO₃ references. And the E_0 is more close to that of MoO₃ sample, indicating the predominance of Mo⁶⁺ in the two catalysts. It is also consistent with XPS analysis. It is therefore concluded that the Fe and Mo centers are no bonding interactions, and their corresponding FeN₄ and MoN₅ sites are spatially separated from one another.

2.2. Electrochemical nitrate reduction performance

The electrochemical NO₃[−] reduction was performed in a customized H-type electrolytic cell in an alkaline solution containing 0.1 M KNO₃ and 1 M KOH at room temperature and atmospheric pressure. The NH₃ produced was quantified by ultraviolet–visible (UV–Vis) extinction spectrophotometry based on indophenol blue spectrophotometric method (IBS). In addition, other residual products such as hydrogen and NO₂[−] intermediate were respectively quantified by gas chromatography and the Griess test respectively. Calibration curves for spectrophotometric tests are provided in Figs. S12 and S13. More details on the electrochemical experiments are available in “Methods”.

The linear sweep voltammetry (LSV) polarization curves of Fe-Mo DSAC (Fig. 3a), Mo and Fe SACs show an enhanced current density relative to that of pure N-C support, indicating the catalytic activity of the metal sites toward the reduction of NO₃[−]. As the materials involve pyrolysis, the process often leading to the formation of defective carbon with catalytic activity [40,41], we also investigated the electrocatalytic properties of the pure N-C support pyrolyzed at 650 °C. The pure N-C support exhibits only < 100 mA/cm² under the studied potentials, significantly lower than that of Fe-Mo DSAC (nearly 300 mA/cm² at −0.98 V vs. RHE). Also, a relatively low NH₃ yield rate was obtained, starting at 0.05 mg_{NH3} h^{−1} cm^{−2} at −0.28 V vs. RHE, increasing to 1.57 mg_{NH3} h^{−1} cm^{−2} at −0.68 V vs. RHE, and reaching a maximum of only 1.67 mg_{NH3} h^{−1} cm^{−2} at −0.98 V vs. RHE. These results indicate a limited reactivity of defective carbon. Mo and Fe SAC provide maximum NH₃ yield rates of 4.78 and 6.45 mg_{NH3} h^{−1} cm^{−2}, respectively at −0.68 V vs. RHE, which are much higher than the 1.57 mg_{NH3} h^{−1} cm^{−2} yield rate exhibited by the N-C support alone at that potential (Fig. 3b).

Fe-Mo DSAC provides an exceptionally high NH₃ yield rate of up to 13.56 mg_{NH3} h^{−1} cm^{−2} at −0.78 V vs. RHE, which is 3.6 times and 2.4 times of that of Mo SAC and Fe SAC, respectively, suggesting synergy

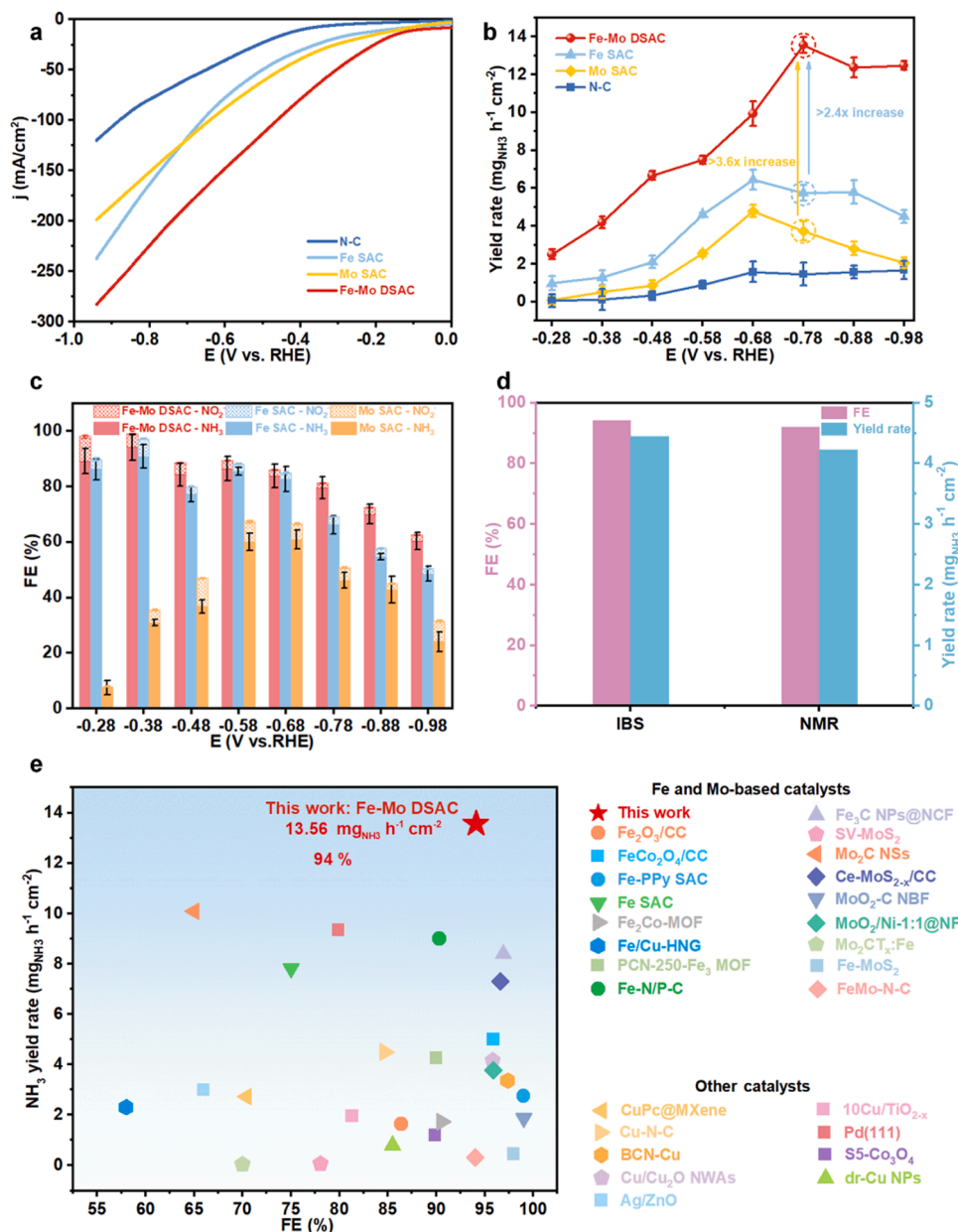


Fig. 3. (a) LSV curves for the N-C substrate, Mo SAC, Fe SAC, and Fe-Mo DSAC in 1 M KOH electrolyte with 0.1 M KNO₃. (b) NH₃ yield rates for the N-C substrate, Mo SAC, Fe SAC, and Fe-Mo DSAC in 1 M KOH electrolyte with 0.1 M KNO₃ at various applied potentials. (c) FE for NH₃ and NO₂ at various applied potentials for the Mo SAC, Fe SAC, and Fe-Mo DSAC in 1 M KOH electrolyte with 0.1 M KNO₃. (d) ¹⁵NH₃ yield rate and FE for NH₃ of Fe-Mo DSAC at -0.38 V vs RHE in 1 M KOH and 0.1 M K¹⁵NO₃ determined by IBS and ¹H NMR. (e) Comparison of the NO₃RR performance metrics (NH₃ yield rate and FE for NH₃) of Fe-Mo DSAC in this work with other recently reported catalysts [7,29,30,43–63]. In (b) and (c), the mean values from three trials using different batches of the same catalyst are plotted, with error bars representing the standard deviation.

between the Mo and Fe sites in Fe-Mo DSAC. The synergy is confirmed by the higher current density and higher ammonia yield rate (by up to 4.3 mg_{NH₃} h⁻¹ cm⁻²) obtained with Fe-Mo DSAC as compared with a physical mixture of Fe SAC and Mo SAC (Figs. S14 and S15; and “Cathode preparation” section in SI). A high FE for NH₃ is achieved as well for the Fe-Mo DSAC, especially at a low overpotential, reaching up to 94% at -0.38 V vs. RHE (Fig. 3c and Fig. S16). In comparison, at this potential, the FE for NH₃ is 91% for Fe SAC, whereas it is only 31% for Mo SAC. This observation underscores that Fe SAC is a desirable electrocatalyst for NO₃RR to produce NH₃. This finding aligns with a high-throughput DFT calculations study, which indicates that Fe SAC exhibits excellent selectivity for NH₃ formation [42]. These results demonstrate that the Fe-Mo DSAC provides both high activity and high selectivity toward NH₃.

The relatively low FE for NH₃ with the Mo SAC is attributed to the formation of byproducts: in addition to H₂, NO₂ accounts for a relatively large proportion of current density. For instance, the NO₂ yield rate is 4.75 mg_{NO₂} h⁻¹ cm⁻² at -0.68 V vs. RHE (Fig. S17) accounts for FE of 6.0%. In contrast, with the Fe-Mo DSAC, an FE for NO₂ of only < 2% was at -0.68 V vs. RHE. This suggests that Fe in the DSAC promotes further conversion of NO₂ that would have otherwise remained unconverted with a Mo SAC alone. This hypothesis is further confirmed by comparatively performing NO₂ reduction reaction (NO₂RR) experiments on Fe SAC, Mo SAC and Fe-Mo DSAC, as presented in Fig. S18. Notably higher NH₃ yield rates and FE are achieved with Fe-Mo DSAC in NO₂RR compared to NO₃RR under various studied potentials, indicating NO₂ as the intermediate. Moreover, in comparison to Mo SAC, Fe SAC exhibits remarkably elevated NH₃ yield rate and FE in NO₂RR as opposed to

NO₃RR. This reinforces that the Fe single sites in DSAC contribute to an enhanced conversion of NO₂ reduction following the generation of NO₂ from NO₃ catalyzed by Mo single sites. This role of Fe in the DSAC is consistent with the higher NH₃ yield rate and FE for NH₃ exhibited by the Fe SAC compared with the Mo SAC over the entire potential range from -0.28 to -0.98 V vs. RHE (Fig. 3b–c). Taken together, the Mo and Fe sites of DSAC appear to work in tandem with the former most effective at catalyzing the formation of NO₂ from NO₃ and the latter aiding further reduction of NO₂ to NH₃.

The process of preparing Fe-Mo DSAC involves ammonium salts in the precursors, such as ammonium molybdate and hydroxylamine hydrochloride, isotope labeling experiments were therefore conducted using proton nuclear magnetic resonance (¹H NMR) spectroscopy to explore the nitrogen sources of the produced NH₃ [64]. The results are presented in Figs. S19–S20. Electrochemical NO₃RR with Fe-Mo DSAC in 1 M KOH using 0.1 M ¹⁴NO₃ or 0.1 M ¹⁵NO₃, revealed characteristic peaks of ¹⁴NH₄⁺ and ¹⁵NH₄⁺ in the post-reaction electrolyte, respectively (Fig. S20). In addition, the NH₃ yield rate and FE at -0.38 V vs. RHE were determined by ¹H NMR using ¹⁵NO₃ and ¹⁴NO₃ as reactants, aligning closely with IBS results (Fig. 3d and Fig. S21). Additionally, post-reaction spectra of the catholyte from a 1 h reaction conducted over Fe-Mo DSAC in 1 M KOH and 0.1 M KNO₃ with no potentials is similar to that of the blank solution of 1 M KOH (Fig. S22). Moreover, a negligible quantity of NH₃ ($0.004 \text{ mg}_{\text{NH}_3} \text{ h}^{-1} \text{ cm}^{-2}$) was detected with IBS at -0.38 V vs RHE after 1 h reaction in NO₃-free 1 M KOH electrolyte (Fig. S22). The above results confirmed that NH₃ originates from NO₃RR and is not due to contamination from the environment or precursors.

As illustrated in Fig. 3e and Table S3, the NH₃ yield rate obtained using the Fe-Mo DSAC ($13.56 \text{ mg}_{\text{NH}_3} \text{ h}^{-1} \text{ cm}^{-2}$) is well beyond other metal-based catalysts reported recently, such as Fe SAC ($7.82 \text{ mg}_{\text{NH}_3} \text{ h}^{-1} \text{ cm}^{-2}$) [65], Pd (111) facet ($9.32 \text{ mg}_{\text{NH}_3} \text{ h}^{-1} \text{ cm}^{-2}$) [43] and FeCo₂O₄ ($4.98 \text{ mg}_{\text{NH}_3} \text{ h}^{-1} \text{ cm}^{-2}$) [44], while maintaining a high NH₃ FE of up to 94%.

The catalytic stability of the Fe-Mo DSAC for NO₃RR was tested over 24 consecutive cycles in the H-type electrolytic cell under the conditions

most optimal for NH₃ selectivity, i.e., applied potential of -0.38 V vs. RHE. As shown in Fig. 4a, the NH₃ yield rate is stable around $4.3 \text{ mg}_{\text{NH}_3} \text{ h}^{-1} \text{ cm}^{-2}$ with a standard deviation of $0.5 \text{ mg}_{\text{NH}_3} \text{ h}^{-1} \text{ cm}^{-2}$, and the FE fluctuates around 89.1% with a standard deviation of 5.6%. Thus, the catalyst exhibits largely stable performance. STEM imaging and EDS mapping of the Fe-Mo DSAC following the stability test show that Fe and Mo elements were uniformly dispersed on the N-C support without forming nanoparticles or clusters (Fig. 4b–f). Moreover, HAADF-STEM image of the Fe-Mo DSAC following the stability test (Fig. 4g and Fig. S23) shows single metal atoms well dispersed across the catalyst sample. To assess the stability of FePc within the Fe-Mo DSAC under high overpotential after the test, XANES and EXAFS spectra were employed to elucidate the chemical states and coordination environment of Fe atom. As depicted in Fig. S24a, the XANES profile of the Fe K-edge in Fe-Mo DSAC after stability test closely resembles that of the original Fe-Mo DSAC, indicating the enduring stability of the electronic states and spatial configuration of FePc. Similarly, the Fourier-transformed (FT) Fe K-edge EXAFS profile of the Fe-Mo DSAC after the stability test (Fig. S24b) reveals a dominant peak around 1.6 \AA , attributed to Fe-N coordination. Notably, no discernible Fe-Fe bond is evident, indicating that FePc does not form any noticeable Fe particles. To evaluate the chemical states of the metallic elements in Fe-Mo DSAC after the stability test, XPS analysis was performed and is presented in Fig. S25. High-resolution XPS spectra for Fe 2p and Mo 3d of Fe-Mo DSAC were obtained. In comparison with the pretest state (Fig. S9), the tested Fe-Mo DSAC exhibited two diffusive broad peaks at 710 eV and 724 eV, corresponding to Fe 2p_{3/2} and Fe 2p_{1/2}, respectively. In addition, the Fe 2p region was fitted to contributions from different oxidation states of Fe, demonstrating a close resemblance to the pretest state, indicating that the chemical states of Fe element remain similar. Similarly, the Mo 3d XPS spectra closely mirrored that of the initial catalyst, providing further evidence of the robust durability of the Fe-Mo DSAC. Moreover, the element content of Fe-Mo DSAC after stability test was analyzed by ICP and XPS characterization, as presented in Table S1 and Table S4. The results indicate that element content such as Fe, Mo

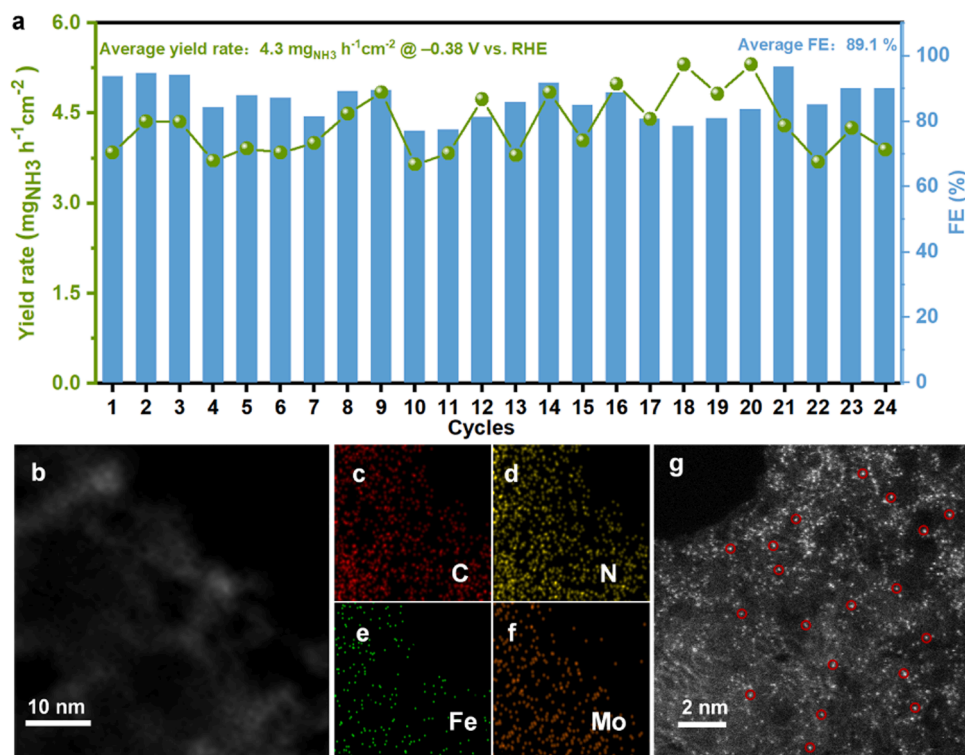


Fig. 4. (a) Stability test of the Fe-Mo DSAC over 24 consecutive electrochemical cycles at -0.38 V vs. RHE. NH₃ yield rate and FE for NH₃ are plotted for each cycle. (b) STEM image and corresponding element maps of (c) C, (d) N, (e) Fe, (f) Mo and (g) atomic-resolution HAADF-STEM image of Fe-Mo DSAC after the stability test.

and N are well-maintained after the stability test.

2.3. Synergistic Mechanism of Fe-Mo DSAC

To further elucidate the catalytic synergy of Fe and Mo sites of Fe-Mo DSAC in the NH_3 production from NO_3^- reduction, we used a combination of in-situ Raman scattering and in-situ FTIR spectroscopy for real-time probing under an applied potential. Details of methodology are provided in SI sections 1.2 and 1.3. Raman scattering spectra of Fe-Mo SAC, Fe SAC and Mo SAC were monitored under electrochemical conditions (Fig. 5a–c). Raman peaks at 998 and 1050 cm^{-1} corresponding to NH_3 and NO_3^- , respectively, were observed. For Fe-Mo DSAC, the characteristic peak of NH_3 appears at a lower onset potential of -0.28 V vs. RHE and then become sharper and more prominent with further increase in the overpotentials. In contrast, for Fe SAC and Mo SAC, the NH_3 peak emerges only at a higher overpotential of -0.38 V vs. RHE with less pronounced peak intensities. The more positive onset potential of the peak relative to NH_3 on Fe-Mo DSAC further indicates the presence of catalytic synergy on Fe-Mo DSAC toward the NO_3^- reduction.

Moreover, the spectra acquired with Fe-Mo DSAC also show peaks at 336 and 593 cm^{-1} at more negative potentials $< -0.28\text{ V}$ vs. RHE (Fig. 5a). These peaks are observed individually for spectra obtained with Mo SAC and Fe SAC, respectively, at potentials $< -0.38\text{ V}$ vs. RHE (Fig. 5b–c). Since Raman spectra acquired with Fe-Mo DSAC in a NO_3^- -free 1 M KOH electrolyte do not exhibit similar peaks (Fig. S26), these peaks cannot be attributed to newly formed metal oxide species or electrolyte OH^- absorption on Mo SAC, Fe SAC and Fe-Mo DSAC. Alternatively, these peaks can be assigned to the oxygenated and nitrogenous intermediate species formed on the metal sites, specifically

Mo=O with a stretching vibration at 336 cm^{-1} and Fe-N with a stretching vibration at 593 cm^{-1} [66–68]. The observations potentially imply that deoxygenation and hydrogenation of nitrogenous species occur respectively on Mo and Fe sites. This is further verified by DFT calculations, which are presented in a later section.

In-situ FTIR spectroscopy was performed to identify intermediates formed on the Fe-Mo DSAC during NO_3RR (Fig. 5d). These differential spectra were collected while scanning the potential from -0.08 to -0.78 V vs. RHE, NO_3RR can easily occur below -0.08 V vs. RHE. When the voltage further decreases, several peaks are clearly observed, originating from nitrogen-containing intermediates. A 1216 cm^{-1} absorption band corresponding to $^*\text{NO}_2$ intermediate is detected at a potential of -0.08 V vs. RHE under the NO_3RR conditions [51,69]. The $^*\text{NO}_2$ peak enhances as the potential became more negative, illustrating that $^*\text{NO}_2$ is a significant intermediate. In addition, the band at 1493 cm^{-1} is ascribed to stretching vibration mode of $^*\text{NO}$, confirming the deoxygenation step during NO_3RR . The peaks from N-H bond are also observed. The broad bands for $^*\text{NH}_3$, $^*\text{NH}_2$ are detected at 1442, 1294 and 1116 cm^{-1} , respectively. These signals of $^*\text{NH}_x$ species reflect the substantial hydrogenation for NH_3 evolution after deoxygenation [51, 70–72]. The peak at $1350\text{--}1380\text{ cm}^{-1}$ merges at high overpotential, assigned to NO_3^- possibly due to the change of local concentration due to highly polarized surface [40]. Moreover, the peak at $\sim 1640\text{ cm}^{-1}$ can be probably attributed to the O-H bending of water originating from aqueous solution [40]. Based on in situ FTIR results, we propose that the reaction pathway of NO_3RR on Fe-Mo DSAC is composed of a tandem process: first deoxygenation of $^*\text{NO}_3$ to NO_2^* , and subsequent hydrogenation of $^*\text{NO}_2$ to NH_3 ($^*\text{NO}_2 \rightarrow ^*\text{NO} \rightarrow ^*\text{NH} \rightarrow ^*\text{NH}_2 \rightarrow ^*\text{NH}_3$).

To further probe the tandem mechanism of functioning of the Fe-Mo

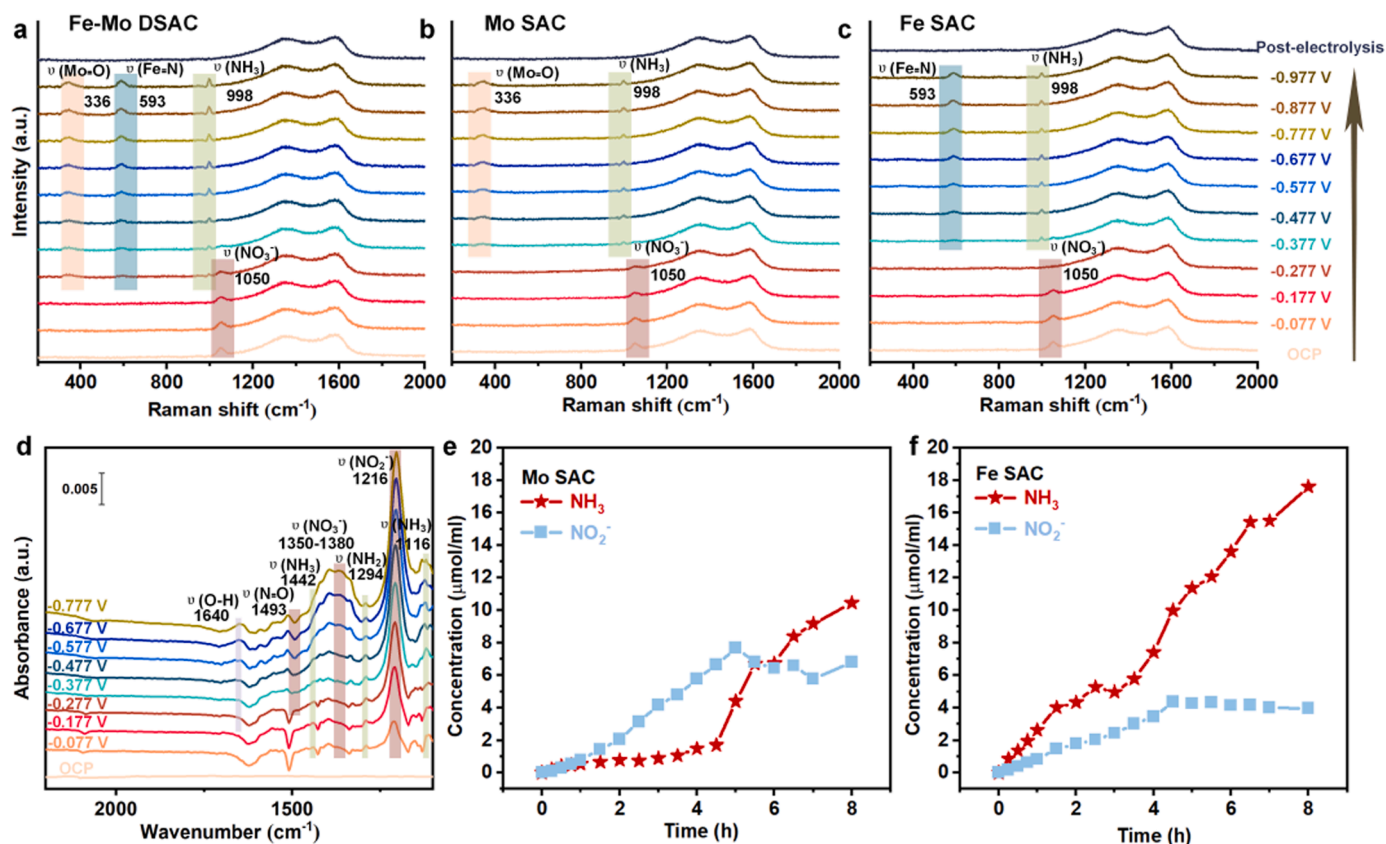


Fig. 5. In-situ Raman spectra of (a) Fe-Mo DSAC, (b) Mo SAC and (c) Fe DSAC and (d) in-situ FTIR spectra of the Fe-Mo DSAC as a function of applied potential in 1 M KOH electrolyte with 0.1 M KNO_3 . Concentration of nitrogen-containing products as a function of reaction time in 1 M KOH electrolyte with 0.1 M KNO_3 at -0.68 V vs RHE with (e) Mo SAC and (f) Fe SAC. The electrolyte was sampled every 15 min for the first hour and every 30 min thereafter until 8 h. A small amount of the electrolyte was extracted each time and tested by the IBS and Griess methods to determine the NH_3 and NO_2^- concentrations, respectively, shown in the plots in e and f.

DSAC, we conducted time-dependent analysis of nitrogen-containing products, specifically NH_3 and NO_2 , in electrochemical reactions on Fe SAC and Mo SAC at -0.68 V vs. RHE (Fig. 5e–f). The electrolyte was sampled every 15 min for the first hour and every 30 min until 8 h. For Mo SAC, it is found that the concentration of NO_2 is higher than that of NH_3 until 5 h, beyond which the NO_2 concentration decreases gradually and is lower than that of NH_3 after 6 h (Fig. 5e). From this time evolution, it appears that NO_2 is produced and gradually accumulated undergoing only limited conversion to NH_3 . The concentration of NO_2 is also higher with Mo SAC than with Fe SAC. On Fe SAC, the concentration of NH_3 is higher than that of NO_2 across all times studied (Fig. 5f). Notably, after 4 h, the NH_3 concentration increased rapidly. This indicates that following the accumulation of NO_2 , conversion to NH_3 is accelerated on the Fe SAC. As observed in Fig. 4e, f, the concentration of reaction intermediate NO_2 exhibits a volcano-shaped profile, characterized by an initial increase and accumulation to a certain level, followed by a gradual decline. The continuously rising NH_3 concentration, coupled with the suppressed NO_2 levels, suggests that NO_2 is also converted to NH_3 in the late stage of the reaction. Comparative results of NO_2 RR and NO_3 RR, depicted in Fig. S18, reveal that both Mo SAC and Fe SAC demonstrate higher NH_3 yield rates in NO_2 RR compared to NO_3 RR under identical conditions. Consequently, as NO_2 accumulates to a certain level and is consumed, it boosts the reaction rate for NH_3 . Taken together, we can deduce that in Fe-Mo DSAC, the Mo sites primarily enable the reduction of NO_3 to NO_2 , then the conversion of NO_2 to NH_3 is primarily realized on Fe sites. Thus, the two metals work in tandem. The higher NH_3 yield rate of Fe-Mo DSAC than Fe SAC can be attributed to the reason that Mo sites in Fe-Mo DSAC promote the formation and accumulation of NO_2 in advance of its further conversion to NH_3 .

According to Arrhenius formulas and calculations [73], $K = \exp[-\frac{1}{k_B T} \Delta G_{\text{max}}(U^0)]$, the rate constant K is exponentially related to the potential-determining step Gibbs free energy change value (PDS ΔG) of the reaction. Therefore, the rate constants K of Fe single sites and Mo single sites in Fe-Mo DSAC are exponentially different, in which the K of Mo is much lower than that of Fe. In order to keep up with the rate of NO_2 consumption by Fe single sites, the metal content of Mo (5.2 wt%) is designed to be higher than that of Fe (0.8 wt%) in Fe-Mo DSAC. Nevertheless, even if the Fe, Mo ratio is changed, it still will not affect the tandem mechanism proposed in the manuscript. It will only affects the reaction rate between Fe and Mo metals, and the change of the reaction rate only speeds up or slows down the reaction process, without causing a change in the tandem mechanism. Meanwhile, to further prove the conclusion on various catalysts with different Fe, Mo ratio, we fixed the Fe content (0.8 wt%) unchanged and adjusted the ratio of the two metals by changing the Mo content to explore the performances.

For Mo SAC with metal contents of 2.97 wt% and 1.06 wt%, and corresponding Fe/Mo metal ratios of 0.27 and 0.75, time-dependent analysis of NH_3 and NO_2 in electrochemical reactions was performed. As shown in Figs. S27 a and b, the time-dependent curves of NO_2 exhibit a similar volcano-shape as observed in Mo SAC (5.2 wt%), with NH_3 gradually increasing as NO_2 decays, confirming NO_2 as the reaction intermediate. In comparison with the initial Mo SAC (5.2 wt%), it is inferred that the decline in metal content leads to a decrease in the reaction rate of Mo SAC, making it challenging to keep up with the rate of NO_2 consumption by Fe SAC. As demonstrated in Figs. S27 c and d, the NH_3 yield rates of Fe-Mo DSAC with Fe/Mo metal ratio 0.27 and 0.75 show noticeable improvement compared with the corresponding Mo SAC. Consequently, Fe single sites in Fe-Mo DSAC also plays a role in converting accumulated NO_2 from Mo single sites to NH_3 . Therefore, varying the Fe, Mo ratio does not impact the proposed tandem mechanism, instead, it affects the reaction rate between Fe and Mo metals, either accelerating or decelerating the reaction process without altering the tandem mechanism.

2.4. DFT calculations

Using DFT calculations, we investigated the interaction between NO_3 RR intermediates and active sites to shed light on the mechanism of action of the Fe-Mo DSAC and the nature of tandem synergy between the metal atoms (Fig. 6a–b). Details of the calculation methods are available in the SI section on Computational methods. Following the characterization results, Fe- N_4 and Mo- N_5 moieties were used as the active center in the calculation model. Fig. 6a–b presents the calculated Gibbs free energy diagrams on the Fe-Mo DSAC (Fe- N_4 and Mo- N_5) for NO_3 to NO_2 and NO_2 to NH_3 process, while Fig. 6c shows the optimized geometries of each NO_3 RR intermediate for each elementary step of NO_3 to NH_3 process. First, adsorbed $^*\text{NO}_3$ is reduced leading to the formation of $^*\text{NO}_2$ on the Fe or Mo atom (Fig. 6c). After the first reduction step (Fig. 6a), the desorption of $^*\text{NO}_2$ from the active site generates NO_2 . This step is energetically uphill with a free energy change value (ΔG) of 0.82 eV on the Fe- N_4 moiety and of 0.54 eV on the Mo- N_5 moiety. Thus, in comparison with the Fe- N_4 moiety, the Mo- N_5 moiety exhibits relatively weaker binding of $^*\text{NO}_2$, and the release of NO_2 intermediate can be relatively facile for Mo sites. Subsequently, remaining adsorbed $^*\text{NO}_2$ undergoes reduction to HNO_2^* and then HNO_2^* undergoes reduction to $^*\text{NO}$ or NO^* . These steps are downhill on the Fe- N_4 and Mo- N_5 . According to the DFT calculations, conversion of NO^* to HNO^* on Fe- N_4 moiety and conversion of $^*\text{NO}$ to $^*\text{NOH}$ on Mo- N_5 moiety, respectively, are the potential-determining steps (PDS) in the reduction of $^*\text{NO}_2$ to $^*\text{NH}_3$ (Fig. 6b and Fig. S28). Moreover, the ΔG of 0.08 eV required for the protonation plus one-electron reduction of NO^* to form HNO^* on Fe- N_4 moiety is much lower than the Gibbs free energy of 0.55 eV for the conversion of $^*\text{NO}$ to $^*\text{NOH}$ on the Mo- N_5 moiety. This points to the favorability of the Fe site for the hydrogenation of $^*\text{NO}_2$ to $^*\text{NH}_3$.

On the Mo- N_5 moiety, intermediate species formed in the conversion of $^*\text{NO}_2$ to $^*\text{NH}_3$ are all bound through the Mo-N bonds (Fig. S28). Nevertheless, $^*\text{NO}_3$ is bound through the Mo=O bond in the reduction of $^*\text{NO}_3$ to $^*\text{NO}_2$, which verifies that the Mo=O bond observed in Raman spectra is related to the deoxygenation of NO_3 to form NO_2 rather than the conversion of $^*\text{NO}_2$ to $^*\text{NH}_3$. Furthermore, we evaluated the Bader charge of Mo- $^*\text{NO}$ and Fe- NO^* configurations (Fig. S29). In Fe- NO^* , the O atom gains 0.6 e^- while N contributes 0.38 e^- , thus the charge difference between N and O is 0.98 e^- . This strong polarization can promote protonation of the O atom of the Fe- NO^* moiety. In contrast, the charge difference between N and O in the Mo- $^*\text{NO}$ configuration is 0.54 e^- , which implies that the N-O bond on the Mo active site is more difficult to be activated. Our calculations verify that the Mo- N_5 sites are the preferred sites for the deoxygenation of NO_3 to NO_2 , while the Fe- N_4 sites catalyze the further hydrogenation of NO_2 to NH_3 . Thus, Fe-Mo DSAC catalyzes the NO_3 RR through this tandem mechanism.

3. Conclusion

In general, we demonstrate tandem catalysis achieved through the cooperation of two metal single atoms for electrochemical NO_3 RR (Fe-Mo DSAC). Specifically, Fe and Mo single atom catalysts work synergistically to accomplish the complete conversion of NO_3 to NH_3 with high activity and selectivity: NO_3 is reduced to NO_2 preferentially on Mo single atom sites, while the NO_2 intermediate, which would otherwise remain unconverted, undergoes further transformation to NH_3 on Fe single atom sites. The Fe-Mo DSAC overcomes the low selectivity of Mo SAC (Faradaic efficiency < 60%) and the relatively low NH_3 yield rate of Fe SAC (< 6.5 $\text{mg cm}^{-2} \text{ h}^{-1}$), exhibiting NO_3 RR performance (13.56 $\text{mg cm}^{-2} \text{ h}^{-1}$, 94%) that surpasses most reported catalysts under similar conditions. Thus, the concept of a DSAC with the metal sites working in tandem is shown to be powerful for catalyzing multi-step reactions. Moreover, the different valence state compositions and proportions of single atom catalysts may also affect the catalytic activity, which possibly deserves further exploration with the help of e.g., in-situ XAS.

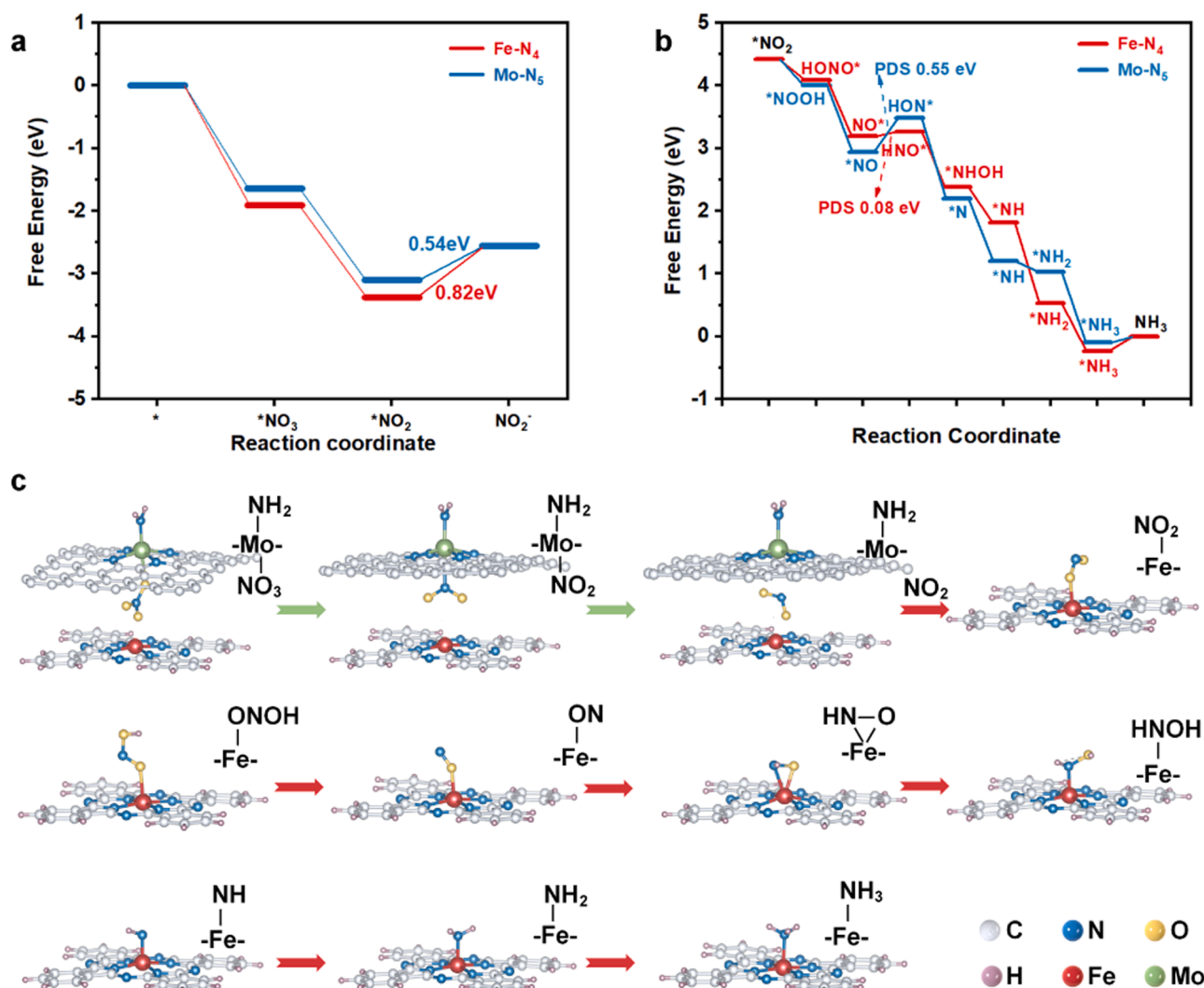


Fig. 6. Gibbs free energy diagrams for (a) NO_3^- to NO_2^- conversion and (b) NO_2 to NH_3 conversion on Fe-Mo DSAC. c Optimized geometries of NO_3RR intermediates for each elementary step of Fe-Mo DSAC.

4. Methods

4.1. Chemicals

Ultra-pure water (resistivity of 18.2 M Ω ·cm), anhydrous ethanol (99.7%, Shanghai Chemical Reagents), glucose (99.5%, RHAWN), ammonium molybdate (99.98%, Aladdin), hydroxylamine hydrochloride (99.99%, Aladdin), iron phthalocyanine (FePc, 98%, Aladdin), N,N-dimethylformamide (99.9%, Aladdin) were used for the preparation of Fe-Mo DSAC, Fe SAC and Mo SAC catalysts. KOH (85%, Shanghai Chemical Reagents), KNO_3 (99%, Shanghai Chemical Reagents), carbon paper (SGL29bc), and Nafion solution (5 wt%, Dupont) were used for electrochemical experiments. Sodium hypochlorite solution (6–14% active chlorine, Aladdin), sodium salicylate (99.5%, Aladdin), sodium nitroferricyanide dehydrate (99%, Aladdin), NaOH (97%, Aladdin) and $^{14}\text{N-NH}_4\text{Cl}$ (99.8%, Aladdin) were used for spectrophotometric NH_3 quantification. H_3PO_4 (99.99%, Macklin), N-(1-naphthyl) ethyldiamine dihydrochloride (98%, Aladdin), and sulfonamide (99%, Aladdin) were used for nitrite quantification. $^{15}\text{N-NH}_4\text{Cl}$ (> 99 atom %, Macklin), D_2O (99.9%, Macklin), maleic acid (99%, J&K), and $^{15}\text{N-nitrate}$ (99 atom %, Aladdin) were used for NH_3 quantification by ^1H NMR.

4.2. Synthesis of N-C

0.72 g glucose was firstly dispersed in 200 mL of ethanol. Similarly, 3.45 g hydroxylamine hydrochloride was ultrasonically dispersed in 200 mL of water. The solution was then added dropwise into the glucose solution, which was later stirred at 70 $^\circ\text{C}$ for 10 h to evaporate water and ethanol. The final products were ground into powder. The precursor powder was placed in a porcelain boat, heated from room temperature to 650 $^\circ\text{C}$ at a rate of 5 $^\circ\text{C}/\text{min}$ under Ar atmosphere and kept for 4 h in a tube furnace to attain porous nitrogen-doped carbon (denoted as N-C).

4.3. Synthesis of Fe SAC

100 mg of N-C was poured into 100 mL of N, N-dimethylformamide and dispersed by ultrasonication for 0.5 h to gain a well-dispersed suspension. 10 mg of FePc was then dispersed into the solution, followed by stirring at room temperature for 12 h. Due to the presence of ammonium-based salt in the precursor, the suspended solid was then separated by filtration and respectively washed three times by anhydrous ethanol and ultra-pure water. To ensure that the salt was washed off, the washed liquid from the final step was tested by indophenol blue spectrophotometric method and no NH_3 was detected. The solid was dried at 60 $^\circ\text{C}$. Fe SAC sample was thus obtained.

4.4. Synthesis of Mo SAC

The Mo SAC was synthesized following the same procedure as that for N-C, using only a different precursor, specifically 3.45 g of hydroxylamine hydrochloride and 38.75 mg of ammonium molybdate. The washing step followed the same procedure as that of Fe SAC.

4.5. Synthesis of Fe-Mo DSAC

The Fe-Mo DSAC was synthesized by a two-step process. Hundred milligrams of Mo SAC was poured into 100 mL of N, N-dimethylformamide and treated by ultrasound for 0.5 h to gain a well-dispersed suspension. 10 mg of FePC was then dispersed into the solution followed by stirring at room temperature for 12 h. The washing step followed the same procedure as that of Fe SAC. The suspended solid was then separated by filtration and finally dried at 60 °C. The product thus obtained was denoted as Fe-Mo DSAC.

4.6. Characterization

XRD patterns were collected on a PANalytical X'pert diffractometer using Cu K α radiation. The Fe and Mo content were quantified by inductively coupled plasma–optical emission spectroscopy (ICP–OES) on an IRIS Intrepid II XSP instrument (Agilent 5110). Nitrogen adsorption–desorption isotherms were measured using on a Micromeritics ASAP 2460 apparatus (Quadrascorb SI Automate Surface Area & Pore Size Analyzer) at –196 °C, and specific surface areas were determined by the Brunauer–Emmett–Teller (BET) method. Surface element composition were measured by XPS on a Thermo Scientific K-Alpha X-ray photoelectron spectrometer, and the binding energy was calibrated on the basis of the 284.8 eV peak of carbon (C 1 s). The atomic metal species were imaged on an EM-ARM300F STEM/TEM instrument. The XAS spectra containing XANES spectra and EXAFS spectra at the Fe K-edge and Mo K-edge were collected at the BL11B beamlines at the Shanghai Synchrotron Radiation Facility (SSRF) in Shanghai, China. Before the analysis at the beamline, samples were pressed into thin sheets 1 cm in diameter and sealed using Kapton tape film. The XAFS spectra were recorded at room temperature using a Bruker 5040 4-channel silicon drift detector (SDD). Fe K-edge EXAFS spectra were recorded in transmission mode. Negligible changes in the line shape and peak position of Fe K-edge XANES spectra were observed between two scans collected for a specific sample. The XAFS spectra of these standard samples (FePC, Fe₂O₃, and FeO) were recorded in transmission mode. The spectra were processed and analyzed by the softwares, Athena and Artemis. The atomic Fe and Mo species were imaged by TEM on a FEI Talos F200S instrument, EDS mapping was performed on a JEOL JEM 2100 F instrument and STEM and HAADF-STEM imaging were performed on a JEOL JEM-ARM200F instrument. Samples for electron microscopy were prepared by drop casting the diluted catalyst ink on to a carbon film microgrid.

4.7. Electrocatalytic nitrate reduction tests

The electrochemical experiments were conducted using an electrochemical workstation (CH Instruments, model number CHI760E) and a gas-tight H-cell where the two chambers are separated by a proton exchange membrane (Nafion-117). A platinum foil (2 cm × 2 cm) was used as the counter electrode, while Ag/AgCl was used as the reference electrode. A fifty-milliliter solution of Ar-saturated 1 M KOH and 0.1 M KNO₃ was used as both the catholyte and anolyte. Cyclic voltammograms (CVs) was first performed in the potential range from 0.2 to –0.98 V vs. RHE at a scan rate of 50 mV s^{–1} for 20 cycles. The measured current was normalized to the geometric area (1 cm²). Linear scanning voltammetry (LSV) scans were acquired with a 10 mV s^{–1} scan rate in the potential range from 0.2 to –0.98 V vs. RHE. Electrochemical reactions were conducted at different potentials (–0.28, –0.38, –0.48,

–0.58, –0.68, –0.78, –0.88, –0.98 V vs. RHE) in the form of 1 h chronoamperometric scans. All applied potentials were referenced to RHE using the formula: $E_{\text{RHE}} = E_{\text{Ag/AgCl}} + 0.059 \cdot \text{pH} + 0.197 \text{ V}$. The catalytic stability of Fe-Mo DSAC was measured by subjecting it to 24 consecutive, 1 h chronoamperometric scans (totaling 24 h) at –0.38 V vs. RHE. For cleaning out unreacted and leftover precursors after each test, the H-cell was immersed in deionized water for 10 min and washed thrice. Nitrite reduction was conducted under the same conditions as that of nitrite reduction.

4.8. Ammonia detection and quantification

The generated NH₃ was quantified by the indophenol blue spectrophotometric (IBS) method. For this, three solutions (labeled here as A, B, and C) were prepared. To prepare solution A, 6.404 g sodium salicylate and 1.312 g NaOH were dissolved into 100 mL H₂O; for solution B, 7.5 mL of sodium hypochlorite solution (6–14% active chlorine) and 3.1 g of NaOH were dissolved in 100 mL H₂O; for solution C, 1 g of sodium nitroferrocyanide dehydrate was dissolved into 100 mL H₂O. For analysis, 50 μ L of the post-reaction electrolyte was extracted and diluted by 1 M KOH to an ultimate volume of 4 mL. To this, 320 μ L of solution C, 2.4 mL of solution A, and 800 μ L of solution B were added in order. After allowing this mixture to stand for 2 h under ambient environment, its ultraviolet–visible (UV–vis) extinction spectrum was measured using a Mapada, UV-3100 spectrophotometer. A calibration (absorbance vs. NH₃ concentration) curve for determining NH₃ concentration in the analyte was made by measuring extinction spectra of a series of standard ammonium chloride (NH₄Cl) solutions.

NH₃ produced was also quantified by proton nuclear magnetic resonance (¹H NMR) spectroscopy on a 600 MHz spectrometer using D₂O as a solvent and maleic acid (C₄H₄O₄) as an internal standard. The calibration curve was obtained as follows. First, a certain amount of NH₄Cl was dissolved in 40 mL of 1 M KOH to prepare 50 ppm (by mass), 100 ppm, 150 ppm, 200 ppm, and 250 ppm standard solutions of NH₄⁺. To each, some volume of 4 M hydrochloric acid was added to adjust the pH to the 2–3 range. Then a solution of 100 ppm standard maleic acid was prepared. The prepared solutions of NH₄⁺ was then mixed with 5 mL 100 ppm standard maleic acid, respectively. Finally, 0.5 mL of the above standard solution was mixed with 50 μ L of D₂O and then transferred into an NMR tube for measuring the ¹H NMR spectrum. By analyzing the ratio of signals of the NH₄⁺ and maleic acid peaks in the spectra, we developed a calibration curve (NH₃ concentration vs. NH₄⁺/maleic acid signal ratio). For ¹H NMR analysis of the NH₄⁺ produced by NO₃[–] reduction for 1 h at –0.38 V vs. RHE, we used a procedure similar to that described for measurements of standard spectra.

4.9. ¹⁵N isotope-labeling experiment

A ¹⁵N isotope-labeling experiment was conducted using a solution of 1 M KOH and 0.1 M K¹⁵NO₃ (99 atom %) as the electrolyte. After ¹⁵NO₃[–] electroreduction for 1 h at –0.38 V vs. RHE, NH₄⁺ in the electrolyte was characterized and quantified by ¹H NMR spectroscopy using the same test methods as those used for ¹⁴NH₄⁺ detection and quantification.

4.10. Nitrite detection and quantification

The Griess method was employed to detect and quantify nitrite in the post-reaction electrolyte. For this analysis, 0.1 g of N-(1-naphthyl) ethylenediamine dihydrochloride, 1 g of sulfonamide, and 2.94 mL of H₃PO₄ were dissolved in 50 mL of deionized water to prepare the Griess reagent solution. The electrolyte was diluted to ensure that the nitrite concentration was in the detection range. Then, 1 mL of the Griess reagent solution was added into 1 mL of the post-reaction electrolyte mixed with 2 mL H₂O. After reacting for 10 min, the absorbance of the solution in the 500–600 nm range was measured on a Mapada UV-3100 spectrophotometer. A calibration (absorbance vs. NO₂[–] concentration)

curve for determining NO₂ concentration in the analyte was made by plotting the absorbance at 540 nm as a function of NO₂ concentration for a series of standard KNO₂ solutions. The nitrite concentration was determined from the established calibration curve.

4.11. Current density

The current density, I_c , was calculated as follows:

$$I_c = I_m/S$$

where I_m is the measured current of the cathode. Since the cathode was prepared by coating the catalyst ink onto 1 cm × 1 cm carbon paper, the area, S , was 1 cm².

4.12. Faradaic efficiency

The FEs, in % terms, of NH₃ and NO₂ products were calculated as follows:

$$FE_{NH_3} (\%) = 100 \times (8 \times F \times C_{NH_3} \times V) / (17 \times Q)$$

$$FE_{NO_2} (\%) = 100 \times (2 \times F \times C_{NO_2} \times V) / (46 \times Q)$$

where F is Faraday's constant with a value of 96485 C/mol, C_{NH_3} is the measured NH₃ concentration by the IBS method, C_{NO_2} is the NO₂ concentration, V is the volume of the catholyte, and Q is the total charge passing the electrode.

Author contributions

Jieying Wan, Hao Zhang, and Xiaodong Li conceptualized the project. Xiaodong Li, Hao Zhang and Ji Yang supervised the project. Jieying Wan developed and performed catalyst synthesis. Jieying Wan, Jiageng Zheng, and Bingru Lan conducted the catalytic tests and data analysis. Jieying Wan performed materials characterization with the help of Xiaodong Li, Hao Zhang, Ji Yang, Zhongkang Han, Wentao Yuan, Jiageng Zheng and Bingru Lan. Ji Yang performed the DFT simulation. Jieying Wan, Xiaodong Li, Hao Zhang, and Ji Yang wrote the manuscript and validated the data and revised the manuscript. All authors discussed the results and commented on the manuscript.

CRediT authorship contribution statement

Wan Jieying: Writing – original draft, Methodology, Investigation, Formal analysis, Data curation, Conceptualization. **Zhang Hao:** Writing – review & editing, Visualization, Validation, Supervision, Resources, Project administration, Methodology, Investigation, Funding acquisition, Formal analysis, Data curation, Conceptualization. **Yang Ji:** Writing – review & editing, Visualization, Validation, Supervision, Software, Project administration, Methodology, Investigation, Formal analysis, Data curation, Conceptualization. **Zheng Jiageng:** Software, Investigation, Formal analysis, Data curation. **Han Zhongkang:** Writing – review & editing, Validation, Supervision. **Yuan Wentao:** Writing – review & editing, Visualization, Validation, Supervision. **Lan Bingru:** Methodology, Investigation, Formal analysis, Data curation. **Li Xiaodong:** Writing – review & editing, Visualization, Validation, Supervision, Resources, Funding acquisition.

Declaration of Competing Interest

The authors declare that they have no known competing financial interests or personal relationships that could have appeared to influence the work reported in this paper.

Data Availability

Data will be made available on request.

Acknowledgement

This work was supported by the National Natural Science Foundation of China (51976191, 52276214).

Appendix A. Supporting information

Supplementary data associated with this article can be found in the online version at [doi:10.1016/j.apcatb.2024.123816](https://doi.org/10.1016/j.apcatb.2024.123816).

References

- [1] Y. Liu, L. Huang, Y. Fang, X. Zhu, S. Dong, Achieving ultrahigh electrocatalytic NH₃ yield rate on Fe-doped Bi₂WO₆ electrocatalyst, *Nano Res.* (2021) <https://doi.org/10/gk57pc>.
- [2] Q. Li, J. Wang, Y. Cheng, K. Chu, Zn nanosheets: An earth-abundant metallic catalyst for efficient electrochemical ammonia synthesis, *J. Energy Chem.* 54 (2021) 318–322, <https://doi.org/10/gk5wp6>.
- [3] H.S. Kim, J. Choi, J. Kong, H. Kim, S.J. Yoo, H.S. Park, Regenerative electrocatalytic redox cycle of copper sulfide for sustainable NH₃ production under ambient conditions, *ACS Catal.* 11 (2021) 435–445, <https://doi.org/10/gk57qd>.
- [4] G. Li, H. Lin, Z. Pan, Y. Liu, L. An, Boosting electrocatalytic nitrogen reduction to ammonia in alkaline media, *Int. J. Energy Res.* 45 (2021) 19364–19644, <https://doi.org/10/gk57nw>.
- [5] X. Wang, D. Wu, S. Liu, J. Zhang, X.-Z. Fu, J.-L. Luo, Folic acid self-assembly enabling manganese single-atom electrocatalyst for selective nitrogen reduction to ammonia, *Nano-Micro Lett.* 13 (2021) 125, <https://doi.org/10/gk57rd>.
- [6] G. Wen, J. Liang, Q. Liu, T. Li, X. An, F. Zhang, A.A. Alshehri, K.A. Alzahrani, Y. Luo, Q. Kong, X. Sun, Ambient ammonia production via electrocatalytic nitrite reduction catalyzed by a CoP nanoarray, *Nano Res.* (2021) <https://doi.org/10/gkhd89>.
- [7] L.-X. Li, W.-J. Sun, H.-Y. Zhang, J.-L. Wei, S.-X. Wang, J.-H. He, N.-J. Li, Q.-F. Xu, D.-Y. Chen, H. Li, J.-M. Lu, Highly efficient and selective nitrate electroreduction to ammonia catalyzed by molecular copper catalyst@Ti₃C₂TX MXene, *J. Mater. Chem. A* 9 (2021) 21771–21778, <https://doi.org/10/gpmrrh>.
- [8] J. Guo, P. Chen, Catalyst: NH₃ as an energy carrier, *Chem* 3 (2017) 709–712, <https://doi.org/10/gk4228>.
- [9] X. Yan, D. Liu, H. Cao, F. Hou, J. Liang, S.X. Dou, Nitrogen reduction to ammonia on atomic-scale active sites under mild conditions, *small, Methods* 3 (2019) 1800501, <https://doi.org/10/gk4ddg>.
- [10] J. Wan, J. Zheng, H. Zhang, A. Wu, X. Li, Single atom catalysis for electrocatalytic ammonia synthesis, *Catal. Sci. Technol.* (2022), 10.1039.D1CY01442K. <https://doi.org/10/gnwdtk>.
- [11] J.H. Montoya, C. Tsai, A. Vojvodica, J.K. Nørskov, The challenge of electrochemical ammonia synthesis: a new perspective on the role of nitrogen scaling relations, *ChemSusChem* 8 (2015) 2180–2186, <https://doi.org/10/f279hz>.
- [12] L. Lassaletta, G. Billen, B. Grizzetti, J. Anglade, J. Garnier, 50 year trends in nitrogen use efficiency of world cropping systems: the relationship between yield and nitrogen input to cropland, *Environ. Res. Lett.* 9 (2014) 105011, <https://doi.org/10.1088/1748-9326/9/10/105011>.
- [13] C.J.M. van der Ham, M.T.M. Koper, D.G.H. Hetterscheid, Challenges in reduction of dinitrogen by proton and electron transfer, *Chem. Soc. Rev.* 43 (2014) 5183–5191, <https://doi.org/10/gj34rs>.
- [14] S. Wang, F. Ichihara, H. Pang, H. Chen, J. Ye, Nitrogen fixation reaction derived from nanostructured catalytic materials, *Adv. Funct. Mater.* 28 (2018) 1803309, <https://doi.org/10/ghwgc9>.
- [15] Y. Yao, J. Wang, U.B. Shahid, M. Gu, H. Wang, H. Li, M. Shao, Electrochemical synthesis of ammonia from nitrogen under mild conditions: current status and challenges, *Electrochem. Energy Rev.* 3 (2020) 239–270, <https://doi.org/10/gmbgt9>.
- [16] W. He, J. Zhang, S. Dieckhöfer, S. Varhade, A.C. Brix, A. Lielpetere, S. Seisel, J.R. C. Junqueira, W. Schuhmann, Splicing the active phases of copper/cobalt-based catalysts achieves high-rate tandem electroreduction of nitrate to ammonia, *Nat. Commun.* 13 (2022) 1129, <https://doi.org/10.1038/s41467-022-28728-4>.
- [17] S. Giddey, S.P.S. Badwal, A. Kulkarni, Review of electrochemical ammonia production technologies and materials, *Int. J. Hydrog. Energy* 38 (2013) 14576–14594, <https://doi.org/10/f5k8zw>.
- [18] V. Rosca, M. Duca, M.T. de Groot, M.T.M. Koper, Nitrogen cycle electrocatalysis, *Chem. Rev.* 109 (2009) 2209–2244, <https://doi.org/10.1021/cr800369g>.
- [19] J.G. Chen, R.M. Crooks, L.C. Seefeldt, K.L. Bren, R.M. Bullock, M.Y. Darensbourg, P.L. Holland, B. Hoffman, M.J. Janik, A.K. Jones, M.G. Kanatzidis, P. King, K. M. Lancaster, S.V. Lymar, P. Pfromm, W.F. Schneider, R.R. Schrock, Beyond fossil fuel-driven nitrogen transformations, *Science* 360 (2018) eaar6611, <https://doi.org/10.1126/science.aar6611>.
- [20] Y. Wang, A. Xu, Z. Wang, L. Huang, J. Li, F. Li, J. Wicks, M. Luo, D.-H. Nam, C.-S. Tan, Y. Ding, J. Wu, Y. Lum, C.-T. Dinh, D. Sinton, G. Zheng, E.H. Sargent, Enhanced nitrate-to-ammonia activity on copper–nickel alloys via tuning of

- intermediate adsorption, *J. Am. Chem. Soc.* 142 (2020) 5702–5708, <https://doi.org/10.1021/jacs.9b13347>.
- [21] L. Li, C. Tang, X. Cui, Y. Zheng, X. Wang, H. Xu, S. Zhang, T. Shao, K. Davey, S.-Z. Qiao, Efficient nitrogen fixation to ammonia through integration of plasma oxidation with electrocatalytic reduction, *Angew. Chem. Int. Ed.* 60 (2021) 14131–14137, <https://doi.org/10/gk5wx2>.
 - [22] J. Sun, D. Alam, R. Daiyan, H. Masood, T. Zhang, R. Zhou, P.J. Cullen, E.C. Lovell, A. (Rouhollah) Jalili, R. Amal, A hybrid plasma electrocatalytic process for sustainable ammonia production, *Energy Environ. Sci.* 14 (2021) 865–872, <https://doi.org/10/gk57m3>.
 - [23] A. Wu, J. Yang, B. Xu, X.-Y. Wu, Y. Wang, X. Lv, Y. Ma, A. Xu, J. Zheng, Q. Tan, Y. Peng, Z. Qi, H. Qi, J. Li, Y. Wang, J. Harding, X. Tu, A. Wang, J. Yan, X. Li, Direct ammonia synthesis from the air via gliding arc plasma integrated with single atom electrocatalysis, *Appl. Catal. B: Environ.* 299 (2021) 120667 <https://doi.org/10/gmns6q>.
 - [24] M. Dortsiou, G. Kyriacou, Electrochemical reduction of nitrate on bismuth cathodes, *J. Electroanal. Chem.* 630 (2009) 69–74, <https://doi.org/10.1016/j.jelechem.2009.02.019>.
 - [25] I. Katsounaros, D. Ipsakis, C. Polatides, G. Kyriacou, Efficient electrochemical reduction of nitrate to nitrogen on tin cathode at very high cathodic potentials, *Electrochim. Acta* 52 (2006) 1329–1338, <https://doi.org/10.1016/j.electacta.2006.07.034>.
 - [26] Z. Wang, D. Richards, N. Singh, Recent discoveries in the reaction mechanism of heterogeneous electrocatalytic nitrate reduction, *Catal. Sci. Technol.* 11 (2021) 705–725, <https://doi.org/10.1039/D0CY02025G>.
 - [27] J.-X. Liu, D. Richards, N. Singh, B.R. Goldsmith, Activity and selectivity trends in electrocatalytic nitrate reduction on transition metals, *ACS Catal.* 9 (2019) 7052–7064, <https://doi.org/10.1021/acscatal.9b02179>.
 - [28] P. Li, R. Li, Y. Liu, M. Xie, Z. Jin, G. Yu, Pulsed nitrate-to-ammonia electroreduction facilitated by tandem catalysis of nitrite intermediates, *J. Am. Chem. Soc.* 145 (2023) 6471–6479, <https://doi.org/10.1021/jacs.3c00334>.
 - [29] J. Yang, H. Qi, A. Li, X. Liu, X. Yang, S. Zhang, Q. Zhao, Q. Jiang, Y. Su, L. Zhang, J.-F. Li, Z.-Q. Tian, W. Liu, A. Wang, T. Zhang, Potential-driven restructuring of Cu single atoms to nanoparticles for boosting the electrochemical reduction of nitrate to ammonia, *J. Am. Chem. Soc.* 144 (2022) 12062–12071, <https://doi.org/10.1021/jacs.2c02262>.
 - [30] Y. Wang, W. Zhou, R. Jia, Y. Yu, B. Zhang, Unveiling the activity origin of a copper-based electrocatalyst for selective nitrate reduction to ammonia, *Angew. Chem. Int. Ed.* 59 (2020) 5350–5354, <https://doi.org/10.1002/anie.201915992>.
 - [31] X. Lu, H. Song, J. Cai, S. Lu, Recent development of electrochemical nitrate reduction to ammonia: a mini review, *Electrochem. Commun.* 129 (2021) 107094 <https://doi.org/10/gnx43q>.
 - [32] J. Yang, W. Liu, M. Xu, X. Liu, H. Qi, L. Zhang, X. Yang, S. Niu, D. Zhou, Y. Liu, Y. Su, J.-F. Li, Z.-Q. Tian, W. Zhou, A. Wang, T. Zhang, Dynamic behavior of single-atom catalysts in electrocatalysis: identification of Cu-N₃ as an active site for the oxygen reduction reaction, *J. Am. Chem. Soc.* 143 (2021) 14530–14539, <https://doi.org/10.1021/jacs.1c03788>.
 - [33] L. Han, X. Liu, J. Chen, R. Lin, H. Liu, F. Lü, S. Bak, Z. Liang, S. Zhao, E. Stavitski, J. Luo, R.R. Adzic, H.L. Xin, Atomically dispersed molybdenum catalysts for efficient ambient nitrogen fixation, *Angew. Chem. Int. Ed.* 58 (2019) 2321–2325, <https://doi.org/10/gftj9h>.
 - [34] P. Chen, T. Zhou, L. Xing, K. Xu, Y. Tong, H. Xie, L. Zhang, W. Yan, W. Chu, C. Wu, Y. Xie, Atomically dispersed iron–nitrogen species as electrocatalysts for bifunctional oxygen evolution and reduction reactions, *Angew. Chem. Int. Ed.* 56 (2017) 610–614, <https://doi.org/10.1002/anie.201610119>.
 - [35] L. Jiao, G. Wan, R. Zhang, H. Zhou, S.-H. Yu, H.-L. Jiang, From metal–organic frameworks to single-atom Fe implanted N-doped porous carbons: efficient oxygen reduction in both alkaline and acidic media, *Angew. Chem. Int. Ed.* 57 (2018) 8525–8529, <https://doi.org/10/gdv8q2>.
 - [36] M. Zhang, Y.-G. Wang, W. Chen, J. Dong, L. Zheng, J. Luo, J. Wan, S. Tian, W.-C. Cheong, D. Wang, Y. Li, Metal (Hydro)oxides@Polymer Core-shell strategy to metal single-atom materials, *J. Am. Chem. Soc.* 139 (2017) 10976–10979, <https://doi.org/10.1021/jacs.7b05372>.
 - [37] W. Chen, J. Pei, C.-T. He, J. Wan, H. Ren, Y. Zhu, Y. Wang, J. Dong, S. Tian, W.-C. Cheong, S. Lu, L. Zheng, X. Zheng, W. Yan, Z. Zhuang, C. Chen, Q. Peng, D. Wang, Y. Li, Rational design of single molybdenum atoms anchored on N-doped carbon for effective hydrogen evolution reaction, *Angew. Chem. Int. Ed.* 56 (2017) 16086–16090, <https://doi.org/10.1002/anie.201710599>.
 - [38] P. Peng, L. Shi, F. Huo, C. Mi, A. Wu, S. Zhang, Z. Xiang, A pyrolysis-free path toward superiorly catalytic nitrogen-coordinated single atom, *Sci. Adv.* 5 (2019) eaaw2322, <https://doi.org/10.1126/sciadv.aaw2322>.
 - [39] J. Guo, X. Yan, Q. Liu, Q. Li, X. Xu, L. Kang, Z. Cao, G. Chai, J. Chen, Y. Wang, J. Yao, The synthesis and synergistic catalysis of iron phthalocyanine and its graphene-based axial complex for enhanced oxygen reduction, *Nano Energy* 46 (2018) 347–355, <https://doi.org/10.1016/j.nanoen.2018.02.026>.
 - [40] L. Huang, L. Cheng, T. Ma, J.-J. Zhang, H. Wu, J. Su, Y. Song, H. Zhu, Q. Liu, M. Zhu, Z. Zeng, Q. He, M.-K. Tse, D. Yang, B.I. Yakobson, B.Z. Tang, Y. Ren, R. Ye, Direct synthesis of ammonia from nitrate on amorphous graphene with near 100% efficiency, *Adv. Mater.* 35 (2023) 2211856, <https://doi.org/10.1002/adma.202211856>.
 - [41] L. Cheng, T. Ma, B. Zhang, L. Huang, W. Guo, F. Hu, H. Zhu, Z. Wang, T. Zheng, D.-T. Yang, C.-K. Siu, Q. Liu, Y. Ren, C. Xia, B.Z. Tang, R. Ye, Steering the topological defects in amorphous laser-induced graphene for direct nitrate-to-ammonia electroreduction, *ACS Catal.* 12 (2022) 11639–11650, <https://doi.org/10.1021/acscatal.2c03219>.
 - [42] S. Wang, H. Gao, L. Li, K.S. Hui, D.A. Dinh, S. Wu, S. Kumar, F. Chen, Z. Shao, K. N. Hui, High-throughput identification of highly active and selective single-atom catalysts for electrochemical ammonia synthesis through nitrate reduction, *Nano Energy* 100 (2022) 107517, <https://doi.org/10.1016/j.nanoen.2022.107517>.
 - [43] Y. Han, X. Zhang, W. Cai, H. Zhao, Y. Zhang, Y. Sun, Z. Hu, S. Li, J. Lai, L. Wang, Facet-controlled palladium nanocrystalline for enhanced nitrate reduction towards ammonia, *J. Colloid Interface Sci.* 600 (2021) 620–628, <https://doi.org/10/gk57rf>.
 - [44] J. Li, D. Zhao, L. Zhang, L. Yue, Y. Luo, Q. Liu, N. Li, A.A. Alshehri, M.S. Hamdy, Q. Li, X. Sun, A FeCo₂O₄ nanowire array enabled electrochemical nitrate conversion to ammonia, *Chem. Commun.* 58 (2022) 4480–4483, <https://doi.org/10.1039/D2CC00189F>.
 - [45] J. Li, Y. Zhang, C. Liu, L. Zheng, E. Petit, K. Qi, Y. Zhang, H. Wu, W. Wang, A. Tiberj, X. Wang, M. Chhowalla, L. Lajjaunie, R. Yu, D. Voiry, 3.4% solar-to-ammonia efficiency from nitrate using Fe single atomic catalyst supported on MoS₂ nanosheets, *Adv. Funct. Mater.* 32 (2022) 2108316, <https://doi.org/10/gph659>.
 - [46] P. Li, Z. Jin, Z. Fang, G. Yu, A single-site iron catalyst with preoccupied active centers that achieves selective ammonia electrosynthesis from nitrate, *Energy Environ. Sci.* 14 (2021) 3522–3531, <https://doi.org/10/gnqh53>.
 - [47] Y. Xu, M. Wang, K. Ren, T. Ren, M. Liu, Z. Wang, X. Li, L. Wang, H. Wang, Atomic defects in pothole-rich two-dimensional copper nanoplates triggering enhanced electrocatalytic selective nitrate-to-ammonia transformation, *J. Mater. Chem. A* 9 (2021) 16411–16417, <https://doi.org/10/gph6zq>.
 - [48] E. Murphy, Y. Liu, I. Matanovic, S. Guo, P. Tieu, Y. Huang, A. Ly, S. Das, I. Zenyuk, X. Pan, E. Spoecker, P. Atanassov, Highly durable and selective Fe- and Mo-based atomically dispersed electrocatalysts for nitrate reduction to ammonia via distinct and synergized NO₂⁻ pathways, *ACS Catal.* 12 (2022) 6651–6662, <https://doi.org/10.1021/acscatal.2c01367>.
 - [49] X. Zhao, X. Jia, Y. He, H. Zhang, X. Zhou, H. Zhang, S. Zhang, Y. Dong, X. Hu, A. V. Kuklin, G.V. Baryshnikov, H. Ågren, G. Hu, Two-dimensional BCN matrix inlaid with single-atom-Cu driven electrochemical nitrate reduction reaction to achieve sustainable industrial-grade production of ammonia, *Appl. Mater. Today* 25 (2021) 101206, <https://doi.org/10.1016/j.apmt.2021.101206>.
 - [50] F. Lei, K. Li, M. Yang, J. Yu, M. Xu, Y. Zhang, J. Xie, P. Hao, G. Cui, B. Tang, Electrochemical reduction of nitrate on silver surface and an in situ Raman spectroscopy study, *Inorg. Chem. Front.* 9 (2022) 2734–2740, <https://doi.org/10.1039/D2QI00489E>.
 - [51] X. Zhang, C. Wang, Y. Guo, B. Zhang, Y. Wang, Y. Yu, Cu clusters/TiO₂-x with abundant oxygen vacancies for enhanced electrocatalytic nitrate reduction to ammonia, *J. Mater. Chem. A* 10 (2022) 6448–6453, <https://doi.org/10.1039/D2TA00661H>.
 - [52] Z. Niu, S. Fan, X. Li, J. Yang, J. Wang, Y. Tao, G. Chen, Tailored electronic structure by sulfur filling oxygen vacancies boosts electrocatalytic nitrogen oxyanions reduction to ammonia, *Chem. Eng. J.* 451 (2023) 138890, <https://doi.org/10.1016/j.cej.2022.138890>.
 - [53] J. Yan, P. Liu, J. Li, H. Huang, W. Song, Effect of valence state on electrochemical nitrate reduction to ammonia in molybdenum catalysts, *Chem. Eng. J.* 459 (2023) 141601, <https://doi.org/10.1016/j.cej.2023.141601>.
 - [54] M. Fu, Q. Gou, Z. Ma, Y. Jiang, W. Shen, M. Li, R. He, MoO₂/Ni heterojunction with strong electronic coupling prepared by in-situ phase separation for High-Efficiency nitrate electroreduction to ammonia, *Appl. Surf. Sci.* 643 (2024) 158664, <https://doi.org/10.1016/j.apsusc.2023.158664>.
 - [55] D. Zhu, G. Li, X. Yan, C. Geng, L. Gao, Electrochemical nitrate reduction to high-value ammonia on two-dimensional molybdenum carbide nanosheets for nitrate-containing wastewater upcycling, *Sci. Total Environ.* 878 (2023) 163145, <https://doi.org/10.1016/j.scitotenv.2023.163145>.
 - [56] Y. Lv, S.-W. Ke, Y. Gu, B. Tian, L. Tang, P. Ran, Y. Zhao, J. Ma, J.-L. Zuo, M. Ding, Highly efficient electrochemical nitrate reduction to ammonia in strong acid conditions with Fe₂M-trinuclear-cluster metal–organic frameworks, *Angew. Chem. Int. Ed.* 62 (2023) e202305246, <https://doi.org/10.1002/anie.202305246>.
 - [57] S. Zhang, J. Wu, M. Zheng, X. Jin, Z. Shen, Z. Li, Y. Wang, Q. Wang, X. Wang, H. Wei, J. Zhang, P. Wang, S. Zhang, L. Yu, L. Dong, Q. Zhu, H. Zhang, J. Lu, Fe/Cu diatomic catalysts for electrochemical nitrate reduction to ammonia, *Nat. Commun.* 14 (2023) 3634, <https://doi.org/10.1038/s41467-023-39366-9>.
 - [58] J. Wang, Z. Sun, Y. Li, L. Guo, Y. Wang, C. Fan, Y. Wang, R. Li, X. Zhang, F. Li, Z. Yu, J. Liu, Sulfur vacancy MoS₂ for electrocatalytic reduction of nitrate to ammonia with enhanced selectivity, *J. Alloy. Compd.* 955 (2023) 170199, <https://doi.org/10.1016/j.jallcom.2023.170199>.
 - [59] A.K.K. Padinjareveetil, J.V. Perales-Rondon, D. Zorralová, M. Otyepka, O. Alduhaish, M. Pumera, Fe-MOF catalytic nanoarchitectonic toward electrochemical ammonia production, *ACS Appl. Mater. Interfaces* 15 (2023) 47294–47306, <https://doi.org/10.1021/acsaami.3c12822>.
 - [60] J. Xu, S. Zhang, H. Liu, S. Liu, Y. Yuan, Y. Meng, M. Wang, C. Shen, Q. Peng, J. Chen, X. Wang, L. Song, K. Li, W. Chen, Breaking local charge symmetry of iron single atoms for efficient electrocatalytic nitrate reduction to ammonia, *Angew. Chem. Int. Ed.* 62 (2023) e202308044, <https://doi.org/10.1002/anie.202308044>.
 - [61] X. Liu, T. Xie, Z. Cai, Z. Li, L. Zhang, X. Fan, D. Zhao, S. Sun, Y. Luo, Q. Liu, X. Sun, Fe₃C nanoparticles decorated 3D nitrogen-doped carbon foam as a highly efficient electrocatalyst for nitrate reduction to ammonia, *J. Electroanal. Chem.* 933 (2023) 117295, <https://doi.org/10.1016/j.jelechem.2023.117295>.
 - [62] Y. Luo, K. Chen, G. Wang, G. Zhang, N. Zhang, K. Chu, Ce-doped MoS₂-x nanoflower arrays for electrocatalytic nitrate reduction to ammonia, *Inorg. Chem. Front.* 10 (2023) 1543–1551, <https://doi.org/10.1039/D2QI01798A>.
 - [63] D.F. Abbott, Y.-Z. Xu, D.A. Kuznetsov, P. Kumar, C.R. Müller, A. Fedorov, V. Mougél, Understanding the synergy between Fe and Mo sites in the nitrate reduction reaction on a bio-inspired bimetallic MXene electrocatalyst, *Angew. Chem. Int. Ed.* 62 (2023) e202313746, <https://doi.org/10.1002/anie.202313746>.

- [64] H. Iriawan, S.Z. Andersen, X. Zhang, B.M. Comer, J. Barrio, P. Chen, A.J. Medford, I.E.L. Stephens, I. Chorkendorff, Y. Shao-Horn, Methods for nitrogen activation by reduction and oxidation, *Nat. Rev. Methods Prim.* 1 (1) (2021) 26, <https://doi.org/10.1038/s43586-021-00053-y>.
- [65] Z.-Y. Wu, M. Karamad, X. Yong, Q. Huang, D.A. Cullen, P. Zhu, C. Xia, Q. Xiao, M. Shakouri, F.-Y. Chen, J.Y. Kim, Y. Xia, K. Heck, Y. Hu, M.S. Wong, Q. Li, I. Gates, S. Siahrostami, H. Wang, Electrochemical ammonia synthesis via nitrate reduction on Fe single atom catalyst, *Nat. Commun.* 12 (2021) 2870, <https://doi.org/10.1038/s41467-021-02870-8>.
- [66] A.V. Soldatova, M. Ibrahim, J.S. Olson, R.S. Czernuszewicz, T.G. Spiro, New light on NO bonding in Fe(III) heme proteins from resonance raman spectroscopy and DFT modeling, *J. Am. Chem. Soc.* 132 (2010) 4614–4625, <https://doi.org/10.1021/ja906233m>.
- [67] R. Prabhu B, K. Bramhaiah, K.K. Singh, N.S. John, Single sea urchin-MoO₃ nanostructure for surface enhanced Raman spectroscopy of dyes, *Nanoscale Adv.* 1 (2019) 2426–2434, <https://doi.org/10.1039/C9NA00115H>.
- [68] J. Wei, D. Xia, Y. Wei, X. Zhu, J. Li, L. Gan, Probing the oxygen reduction reaction intermediates and dynamic active site structures of molecular and pyrolyzed Fe–N–C electrocatalysts by In Situ Raman spectroscopy, *ACS Catal.* 12 (2022) 7811–7820, <https://doi.org/10.1021/acscatal.2c00771>.
- [69] N. Meng, Y. Huang, Y. Liu, Y. Yu, B. Zhang, Electrosynthesis of urea from nitrite and CO₂ over oxygen vacancy-rich ZnO porous nanosheets, *Cell Rep. Phys. Sci.* 2 (2021) 100378, <https://doi.org/10.1016/j.xcrp.2021.100378>.
- [70] Z. Tao, C.L. Rooney, Y. Liang, H. Wang, Accessing organonitrogen compounds via C–N coupling in electrocatalytic CO₂ reduction, *J. Am. Chem. Soc.* 143 (2021) 19630–19642, <https://doi.org/10.1021/jacs.1c10714>.
- [71] C. Lv, L. Zhong, H. Liu, Z. Fang, C. Yan, M. Chen, Y. Kong, C. Lee, D. Liu, S. Li, J. Liu, L. Song, G. Chen, Q. Yan, G. Yu, Selective electrocatalytic synthesis of urea with nitrate and carbon dioxide, *Nat. Sustain.* 4 (2021) 868–876, <https://doi.org/10.1038/s41893-021-00741-3>.
- [72] Y. Yao, S. Zhu, H. Wang, H. Li, M. Shao, A spectroscopic study of electrochemical nitrogen and nitrate reduction on rhodium surfaces, *Angew. Chem.* 132 (2020) 10565–10569, <https://doi.org/10.1002/ange.202003071>.
- [73] Y. Jiao, Y. Zheng, M. Jaroniec, S.Z. Qiao, Origin of the electrocatalytic oxygen reduction activity of graphene-based catalysts: a roadmap to achieve the best performance, *J. Am. Chem. Soc.* 136 (2014) 4394–4403, <https://doi.org/10.1021/ja500432h>.